Chemical Engineering Journal 518 (2025) 164426

Contents lists available at ScienceDirect

Chemical Engineering Journal

journal homepage: www.elsevier.com/locate/cej

Catalytic phase transition of cobalt oxide enriched in mesoporous carbon polyhedrons for electrosorption of molybdate oxyanions

Yu-Jen Shih [a,*], Zhi-Lun Wu [a], Ming-Rui Wang [a], Chin-Pao Huang [b]

[a] Institute of Environmental Engineering, National Sun Yat-sen University, Taiwan
[b] Department of Civil and Environmental Engineering, University of Delaware, Newark, DE 19716, USA

ARTICLE INFO

Keywords:
Molybdate
Electrosorption
Imidazole frameworks
Faradaic charge transfer
Co anodization

ABSTRACT

Molybdenum (Mo) emerges both an industrial contaminant and valuable recyclable resources. A *Co*-enriched carbon polyhedron (CoCRD) was synthesized for Mo recovery in an electrosorption system. The effective surface area and dispersion of CoO/Co nanoparticles embedded in mesoporous carbon frameworks were significantly enhanced through pyrolysis of an imidazolate precursor. The catalytic transformation of cobalt oxides contributed to pseudocapacitance, which remarkably increased the adsorption capacity for molybdate oxyanions. Raman spectroscopy and free energy calculations revealed that the anodization-induced CoO-to-Co_3O_4 redox reaction promoted molybdate adsorption via monodentate complexation. The reversibility of CoO sites within carbon texture enabled rapid Mo desorption upon potential reversal, facilitating electrode regeneration. Under an applied potential of +1.0 V (vs. RHE) at neutral pH, CoCRD(700) achieved maximum Mo adsorption capacity, as evaluated by a multilayer isotherm model. CoCRD(700) exhibited high stability in cycling molybdate electrosorption, with strong selectivity over commons anions present in real water samples.

1. Introduction

Molybdenum (Mo) is an essential trace mineral for plant growth and microbial metabolism. In surface and groundwater, Mo concentrations typically remain below 5 μg L^{-1} [1]. However, industrial activities such as metallurgy, plating, and the production of flame retardants, pigment, and semiconductors can introduce Mo contaminants into the environment [2]. Excessive Mo intake can lead to health issues in humans, including anemia, gastrointestinal disturbances, hypothyroidism, and bone and joint deformities, etc. [3] The World Health Organization (WHO) recommends a maximum level of 70 μg-Mo L^{-1} in drinking water [4]. Industrial effluent regulations strictly limit Mo discharge to below 0.6 mg L^{-1} in Taiwan. Mo primarily occurs in water as hexavalent molybdate oxyanions (MoO_4^{2-}), which are not easily removed by conventional hydroxide precipitation in wastewater treatment plants. Current methods for the removal of oxyanions are ion exchange and membrane techniques [5,6], while they are limited by challenges of clogging, fouling, and high costs in regeneration and secondary waste disposal. Molybdate predominantly exists as the divalent anion MoO_4^{2-} at pH levels above 4 (with acidic constants of $pK_{a1} = 3.6$, $pK_{a2} = 3.7$), as shown in Fig. S1. At higher concentrations ($> 10^{-5}$ M) and low pH (< 2), multinuclear complexes such as $Mo_7O_{24}^{6-}$ and $Mo_8O_{26}^{4-}$ can form [7]. As a result, electrostatic attraction-based adsorption is deemed as a fast and effective method for removing these oxyanions. Reported molybdate sorbents include metal oxides [8,9], clay minerals [10,11], and activated carbon [12,13]. Since molybdate remains negatively charged across a broad pH range, modifying sorbent surface functional groups is often necessary to enhance adsorption capacity [14].

Electrosorption, the core mechanism behind capacitive deionization (CDI) process, has gained attention as an energy- and cost-effective method for removing ionic pollutants [15]. The ideally polarizable electrode functions as an electrical capacitor, where counter ions are electrostatically stored within the electrical double-layer (EDL). Ions are captured and released through a simple charging/discharging cycle [16]. When the applied bias is terminated or reversed, the electrode surface is immediately refreshed, recovering the ions in the concentrate. CDI systems commonly utilize carbon-based materials such as activated carbon, carbon fibers, graphene oxide, carbon dots, and Metal organic frameworks (MOFs) [17–19], owing to their high specific surface area, ranging from hundreds to thousands of m^2 g^{-1} (as measured by N_2 adsorption). However, porous carbons may not demonstrate uniform affinity for all ionic species. The surface charge of pristine carbons is

* Corresponding author.
E-mail address: yjshih@mail.nsysu.edu.tw (Y.-J. Shih).

https://doi.org/10.1016/j.cej.2025.164426
Received 12 February 2025; Received in revised form 22 April 2025; Accepted 2 June 2025
Available online 6 June 2025

typically negative due to inherent functional groups, which asymmetrically limits their ability to adsorb anions, even under positive polarity conditions [20]. To augment the treatability of oxyanions, carbon electrodes are generally modified with metals or metal oxides. Under specific electrode potentials, the catalytic phase transformation of metal species introduces additional surface charges, contributing to pseudocapacitance [21]. However, the dispersity and uniformity of these active sites are crucial in determining the electrochemical surface area (ECSA) and overall electrosorption performance.

The MOFs are 3D coordination polymers composed of metal ions and organic linkers arranged in crystalline architectures. MOFs recently emerge as a new class of electrode materials with electrical capacitances that surpass those of traditional materials [22]. MOFs also serve as excellent precursors for the synthesis of metal, metal oxide and carbon composite with long-range structural ordering [23]. Zeolitic imidazolate frameworks (ZIFs), a subclass of MOFs, consist of transition metal ions (Zn^{2+}, Co^{2+}, Fe^{2+}, and Cu^{2+}) and imidazole ligands. In ZIFs, metal ions occupy the lattice sites analogous to silicon in zeolites, with oxygen replaced by imidazole anions. Metal ions act as Lewis acids, coordinating with the aza- and amine-nitrogen atoms of the heterocyclic ring, forming complex polyhedral structures. The particle size of pristine ZIFs typically ranged from the micrometer scale to several hundred nanometers, depending on the solvothermal synthesis conditions. However, upon carbonization under a reduced atmosphere, ZIFs are promising materials for producing highly dispersed metal species – ranging from single atoms to nanometer-sized particles – within a porous, N-enriched carbon matrix [24,25]. In this investigation, a CoZIF with cetyltrimethylammonium bromide (CTAB) template and its derived Co-enriched carbon rhombic dodecahedron (CoCRD) were synthesized. This study represents the first attempt to recover Mo from solution using an electrosorption system. The novelty lies in the magnified adsorption capacity of the mesoporous CoCRD, where in-situ embedded Co oxides facilitate effective Mo adsorption. The improved dispersity of Co sites within the carbon matrix modulates the pH-dependent surface charges of the working electrode. Co conversion to CoO and Co_3O_4 is anticipated to catalytically boost Mo adsorption at elevated potentials. Key characteristics of CoCRD, including ECSA, charge efficiency, impedance, and surface potential, were tuned through the pyrolysis. Under constant applied potentials, Mo adsorption was demonstrated in a membrane CDI kit, where adsorption kinetics, selectivity, cycling stability, and the effects of pH and water matrix composition on performance are evaluated.

2. Experimental section

Detailed methodology, including chemical regents, preparation procedures, characterization techniques, and measurement protocols, is provided in Supporting Information S2. The schematic representation of CoZIF/CTAB and CoCRD synthesis is shown in Scheme 1. Batch electrosorption experiments, using ammonium molybdate tetrahydrate ($(NH_4)_6Mo_7O_{24}\bullet 4H_2O$, Honeywell Fluka) as the Mo source, were conducted in a membrane CDI cell, fabricated from polymethyl methacrylate (PMMA), as illustrated in Fig. S2.

3. Results and discussion

3.1. Characterization

As shown in Fig. 1a, the inclusion of CTAB surfactant during the solvothermal process appears to constrain crystal growth, resulting in smaller average size of 200 nm, compared to conventional ZIF-67 [26]. The inset SEM confirms an average diameter of around 2 μm for CoZIF particles prepared in the absence of surfactant. The synthesized CoZIF/CTAB also exhibits more defined single grains with a rhombic dodecahedron crystal habit, which is attributed to the template effect of the surfactants on the growth of the MOF structure. Upon pyrolysis, Fig. 1b indicates that the CoZIF/CTAB crystal structure undergoes moderate shrinkage after 500 °C heating. Additionally, Co^{2+} nodes in the lattice recrystallize as Co metal uniformly distributed over the carbonized surfaces (i.e., CoCRD(500)), as observed under higher-magnification TEM in Fig. 1c. The inset selected-area electron diffraction (SAED) reveals a hexagonal pattern, signifying retained polyhedral structure. Further increasing temperature to 700 °C (Fig. 1d), these Co crystallites grow into nanoclusters. Atomic ratios of C, N, O, and Co in CoZIF/CTAB are 52.3%, 1.9%, 34.4%, and 11.4%, respectively. Notably, pyrolysis under an N_2 gas flow promotes N inclusion in CoCRD(500). The earlier release of O compared to N may transiently increase the relative N percentage at intermediate temperatures However, a notable reduction in O (3.2%) and N (1.2%) contents in CoCRD(700) due to volatilization, alongside an increase in C (87.8%), reflects the progressive carbonization of ZIF polymers into inorganic carbons [23]. The average particle diameter of Co reaches around 10 nm, embedded in the carbon matrix of CoCRD(700) (Fig. 1e). SAED recorded from the Co particles displays clear concentric rings, confirming their polycrystalline nature. The mixed lattice pattern in Fig. 1f demonstrates a d-spacing of 0.204 nm orientated in (1 1 1) plane for Co metal [27], surrounded by the laminar (0 0 2) plane of carbon with a basal spacing of 0.34 nm at the particle fringes. Elemental mappings in Fig. 1g show highly dispersed C and N signals throughout CoCRD(700). Meanwhile, O signals are particularly localized around the Co clusters, indicating partial oxidation of Co on the metallic cores (Fig. S3a).

The effect of pyrolysis on the crystal structure of CoCRD is analyzed by X-ray diffraction, as shown in Fig. 2a. The XRD pattern of the CoZIF/CTAB resembles that of a typical ZIF-67 sample [28], which remains stable at temperatures below 400 °C. Characteristic peaks of CoZIF disappear as the temperature rises above 500 °C, confirming the complete decomposition of the imidazole compound into amorphous carbon. A gradually evolved peak at $2\theta = 26.2^{o}$ corresponds to the formation of graphitic (0 0 2) plane in carbon (Hexagonal, P63mc(186)) [29]. Concurrently, serial planes of Co metal (Cubic, Fm3m(225)), including (1 1 1), (2 0 0), and (2 2 0) at 44.2^{o}, 52^{o}, and 76.3^{o}, respectively [30], become sharper with increasing temperature. These crystallized structures demonstrate that Co^{2+} ions chelated in the

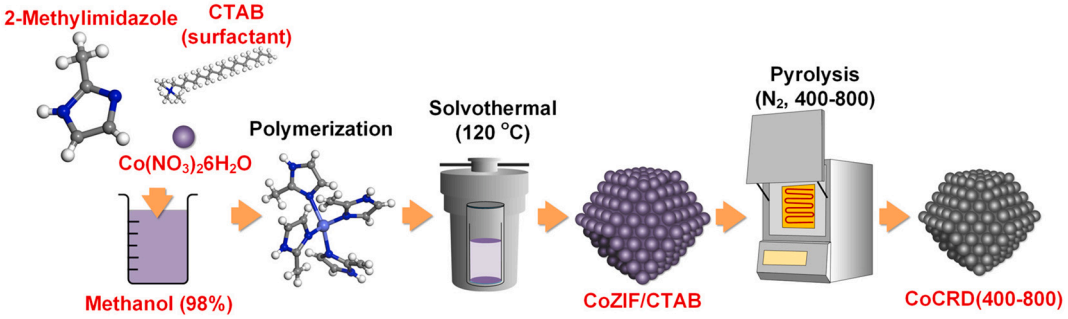

Scheme 1. Procedure of synthesizing CoZIF/CTAB and CoCRD.

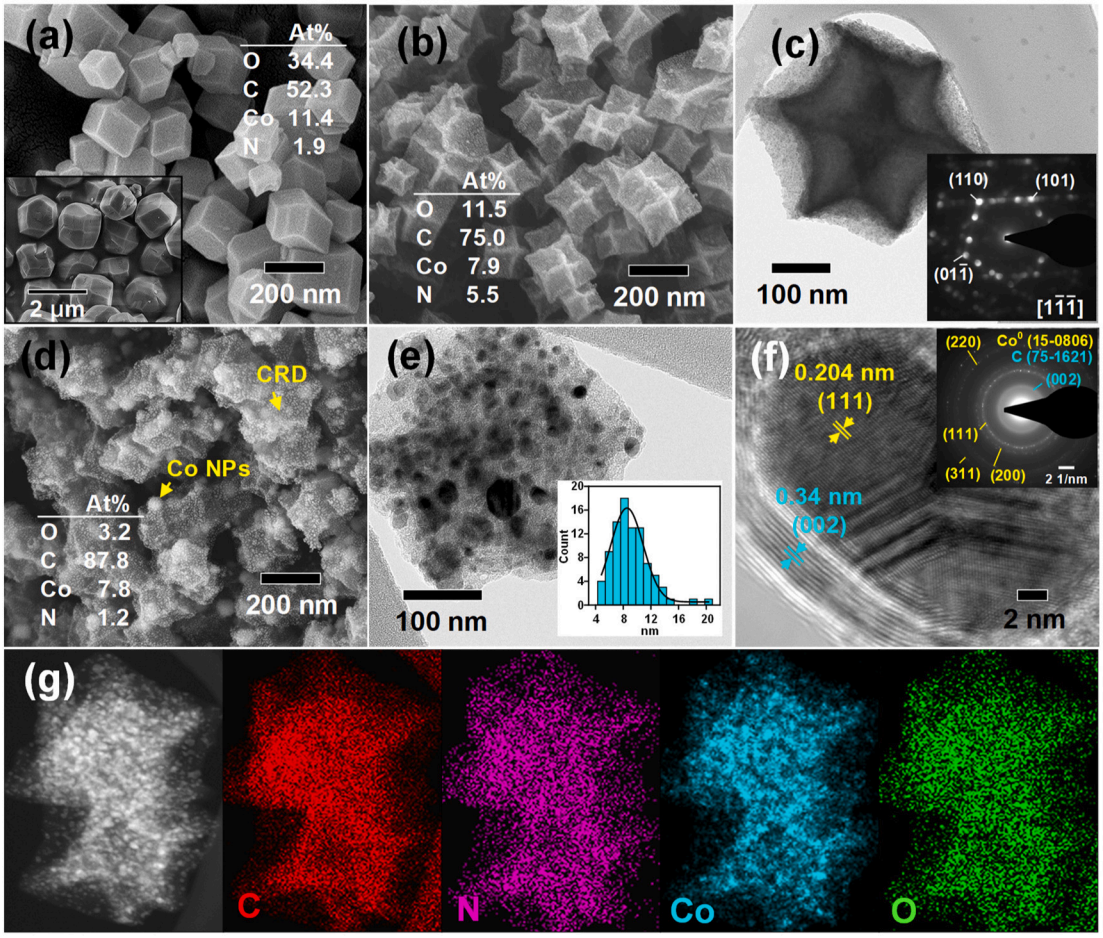

Fig. 1. (a) SEM image of CoZIF/CTAB. (b) SEM and (c) TEM analyses of CoCRD(500); (d) SEM and (e) TEM analyses of CoCRD(700) with (f) Co NPs embedded in the carbon matrix under HRTEM observation. (g) Elemental mappings for CoCRD(700).

polymerized framework are transformed into a composite, with Co metal incorporated into the carbon skeleton. Thermogravimetric analysis (TGA) of CoZIF/CTAB in Fig. 2b indicates a sharp weight drop beginning above 400 °C, with the maximal derivative of mass loss occurring at 500 °C. The total mass loss reaches around 60% within the temperature range of 450–700 °C. This thermal behavior signifies the extent of imidazole carbonization, during which the transformation of CoZIF into Co metal/oxide embedded in a carbon matrix takes place, as observed from XRD analysis.

The BET-specific surface area (S.S.A.) of CoZIF/CTAB reaches 1227 $m^2\ g^{-1}$, as determined by N_2 adsorption in Fig. 2c. This value slightly decreases to 1050 $m^2\ g^{-1}$ after heating to 400 °C, but drops to 69 $m^2\ g^{-1}$ at 500 °C. The sharp decline in S.S.A. is attributed to the decomposition of the 3D organic linkers, as observed on XRD analysis, indicating that the imidazolate crystallinity primarily contributes to the high porosity of CoZIF. Based on the adsorption isotherms, the original CoZIF/CTAB displays a predominantly microporous nature. In contrast, the emergence of an H4-type hysteresis loop (IUPAC classification) indicates the development of mesoporous carbon in CoCRD [31], despite a reduction in overall surface area. Further elevating temperature maximizes the S.S.A. of pyrolyzed carbon to 281 $m^2\ g^{-1}$ for CoCRD(700). The pore size distribution in Fig. 2d shows an average size of 2.2 nm for CoZIF/CTAB, which evolves into a bimodal distribution in CoCRD(700), featuring mesopores of 5.4 nm and macropores of approximately 100 nm [32]. This pore expansion can be explained by the pillaring effect of Co oxides that nucleated, grew, and intercalated in-situ within the carbon texture during carbonization. (As shown in Fig. S3b, CoZIF exhibits a similar specific surface area but a higher proportion of macropores, compared to CoZIF/CTAB, highlighting the influence of CTAB additive.) Raman spectra provide insights into the transition of functional groups during pyrolysis at varied temperatures, as shown in Fig. 2e. The evolution of the carbon structure is evidenced by the two characteristic vibrations of disorder sp^3-hybrid defects (D) at 1302 cm^{-1} and sp^2-hybrid graphitic structure (G) at 1571 cm^{-1} [33]. The relative intensity of I_D/I_G increases from 1.26 to 1.92 as the temperature rises from 400 to 700 °C, indexing greater disorder in the carbon lattice. A decrease in I_D/I_G (1.25) at 800 °C suggests the onset of graphitization in CoCRD at higher temperature. On the other hand, vibrations of cobalt oxide, identified with broad bands at 515 and 683 cm^{-1} for fcc-CoO [34], occur at temperatures above 600 °C. This result aligns with the elemental mapping, which confirms the formation of a partially oxidized layer around the Co cores.

Fig. 2f displays the full XPS spectra of the derived CoCRD, with binding energies around 285, 400, 530, and 780 eV for quantifying C 1s, N 1s, O 1s, and Co 2p orbitals, respectively [35]. The chemical states of the selected elements were further examined through deconvolution of the corresponding peaks, as demonstrated in Fig. 2g – 2j. In organic framework, cobalt primarily exists as divalent Co^{2+} ions, as evidenced by binding energies of 781.4 and 797.2 eV at $2p_{3/2}$ and $2p_{1/2}$ bands, respectively. Through pyrolysis to CoCRD(700), an additional zero-valent Co^0 state forms, determined by binding energies of 779.6 and 795.2 eV at $2p_{3/2}$ and $2p_{1/2}$ bands, respectively, accompanied by a reduced intensity of Co^{II} state [36]. The proportion of Co^0 within cobalt states reaches 58%, corroborating again the recrystallization of Co^{2+} nodes into metallic Co nanoparticles, which are enveloped by a thin oxidized CoO film. The signals of sp^2 (C—C) and sp^3 (C=C) carbon bonds

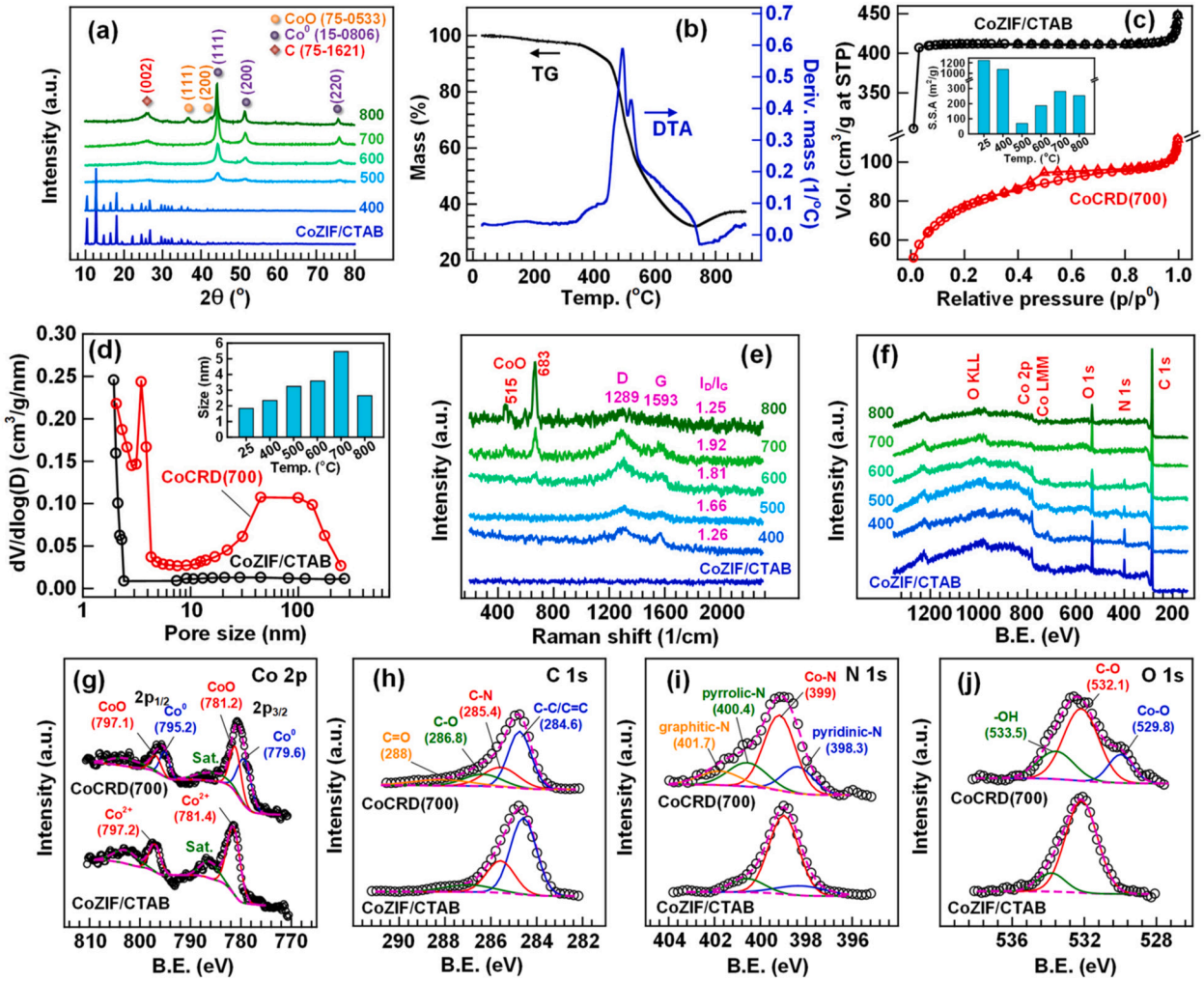

Fig. 2. (a) XRD patterns of CoZIF/CTAB treated with different pyrolysis temperatures. (b) Thermal analysis of CoZIF/CTAB. (c) BET isotherms and (d) pore size distributions of CoZIF/CTAB and CoCRD(700). (e) Raman spectra and (f) XPS of CoZIF/CTAB-derived electrodes. Deconvolution of XPS at binding energies of (g) Co 2p, (h) C 1s, (i) N 1s, and (j) O 1s orbitals.

at 284.6 eV, overlapping with C—N at 285.4 eV, in C 1s spectra are characteristic of the imidazole structure. Additional oxygen functional groups in CoCRD, such as 16% of C—O (286.8 eV) and 12% of C═O (288 eV), are ascribed to mild oxygenation of the derived carbon [37]. The N 1s region shows the developed graphitic-N (401.7 eV) and Co—N (399 eV) bonds, indicating the integration of N atoms into the graphitized carbon, as pyridinic-N (398.3 eV) and pyrrolic-N (400.4 eV) groups remain [38]. Furthermore, the CoO thin film is also evidenced by distinct Co—O (529.8 eV) and Co-OH (533.5) bonds found in the O 1s orbital.

3.2. Electrochemical analysis

The voltammetry curves of CoZIF/CTAB and CoCRD(700), presented in Fig. 3a and b, respectively (1 M NaOH, 10–100 mV s^{-1}), demonstrate a notable enhancement in the current density following the complete carbonization of the ZIF framework. Ideally, the voltammetric response arises from two primary components: the surface-controlled EDL and the diffusion-controlled currents. The EDL current reflects ion storage in the non-faradaic capacitance, while faradaic currents result from electron transfer reactions, such as metal state transitions or redox processes involving chemical species in the electrolyte. For Co-based pseudocapacitor, the diffusive current arises from the reversible phase transformation of Co(II) to Co(III) or Co(IV) within CoO_x at corresponding overpotentials [39]. The specific double-layer capacitance (C_{dl}, F g^{-1}) quantifies the surface charges (σ, coulomb) per unit potential variation ($\varnothing$, volt), which determines the EDL current (I_{dl}) proportional to the scan rate (v, V s^{-1}):

$$C_{dl} = \frac{d\sigma}{d\varnothing} = \frac{Idt}{dE} = \frac{I_{dl}}{v} \tag{1}$$

The redox currents governed by diffusion mechanisms are evaluated as a function of $v^{1/2}$ based on potential step principles. Therefore, the total capacity of the MOF-derived materials (C_{tot}) encompasses charges accumulated into two differently weighted parts [40,41]:

$$C_{tot} = C_{dl} + C_{diff} \tag{2a}$$

$$I_{tot} = I_{dl} + I_{diff} = k_1 v + k_2 v^{1/2} \tag{2b}$$

where factors k_1 and k_2 represent the slope and intercept, respectively, obtained from the linearity of $I_{tot}/v^{1/2}$ against $v^{1/2}$ (as shown in the inset). After weighting, the component $k_2 v^{1/2}$ defines the contribution of redox reactions to the total voltammetric current. As shown in Fig. 3c and d, the faradaic pseudocapacitance (C_{diff}) constitutes approximately 59% of the total current density in CoZIF/CTAB. This value reduces significantly to 42% in CoCRD(700), suggesting an expansion of the EDL surfaces available for ion storage. Additionally, the specific capacitance of the graphite substrate (C_S) was estimated to be 11 μF cm^{-2} (Fig. S4)

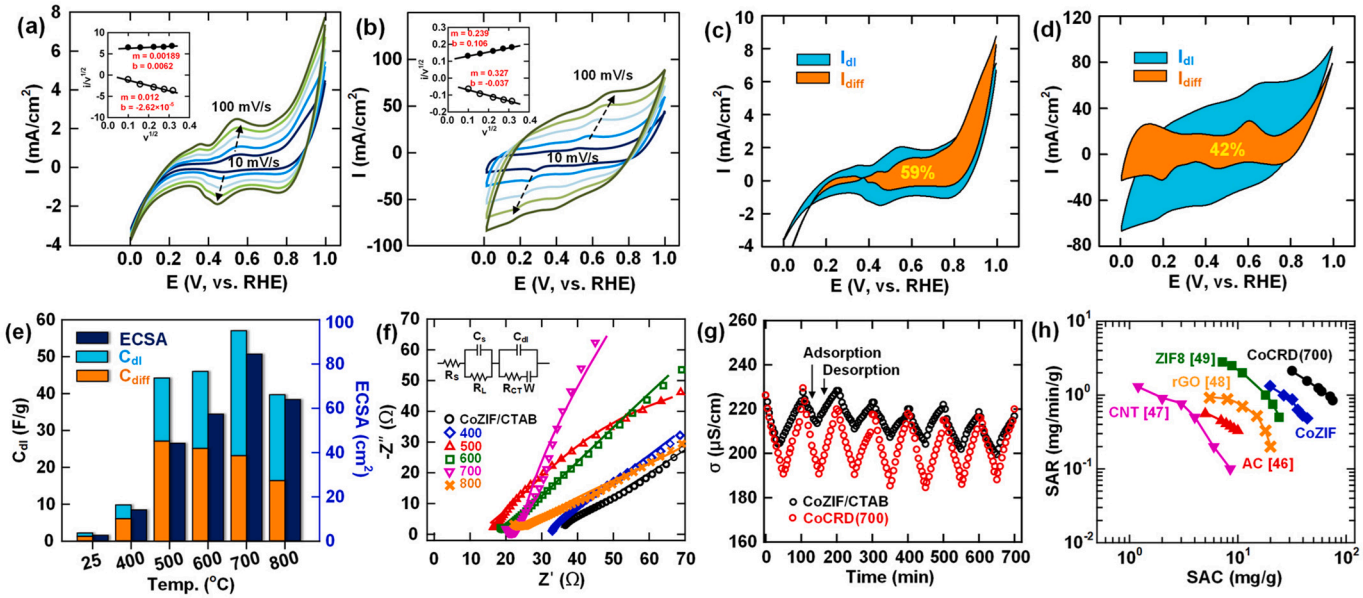

Fig. 3. Voltammetric analyses of (a) CoZIF/CTAB and (b) CoCRD(700), with diffusive and capacitive currents derived from CVs of (c) CoZIF/CTAB and (d) CoCRD (700) (scan rate = 100 mV s^{-1}, 1 M NaOH). Effects of pyrolysis temperature on (e) electrical double-layer capacitance and ECSA, (f) impedance of the CoZIF/CTAB-derived electrodes. (g) Cycling CDI process with an applied bias of 1.2 V for adsorption and 0 V for desorption of NaCl (220 μS cm^{-1}). (h) Ragone plots for carbon electrodes, the data for AC, CNT, rGO, and ZIF-8 carbon materials are reproduced from ref. [46–49].

[42], based on the relation $C_S = \frac{C_{dl,G}}{A_G}$, where $C_{dl,G}$ defines EDL capacitance of graphite and A_G is the geometric area (0.6 cm^2). The ECSA of the MOF-derived electrodes was then obtained by normalizing their EDL capacitances with the graphite reference value, C_S ($ECSA = C_{dl}/C_S$) [43]. The calculated results are summarized in Fig. 3e. The effective surface area follows the same trend to C_{dl}, which is substantially enhanced as the pyrolysis temperature increases beyond 500 °C. The ECSA reaches its maximum value of 84.5 cm^2 for CoCRD(700), nearly 40 times greater than that of CoZIF/CTAB (2.65 cm^2). Voltammetry in molybdate solution was also conducted, as shown in Fig. S5, to clarify the contribution of Mo(VI) redox reactions to the ECSA measurement. The capacitance profiles obtained in the presence of Mo salts were comparable to those measured in NaOH electrolyte alone, with ECSA and C_{diff} proportion reaching 2.57 cm^2 and 53% for CoZIF/CTAB, and 68 cm^2 and 43% for CoCRD(700), respectively. These results indicate that the redox activity of incorporated Co sites does not contribute to the degradation of the adsorbed Mo(VI), and that molybdate remains electrochemically inert under testing potentials. Fig. 3f depicts Nyquist plots obtained from impedance analysis at an anode potential +1.0 V, fitted with the modified Randles circuit in the inset [44]. The resulting parameters, used to specify resistive behaviors of pseudocapacitor, are reported in Table S2. The semicircle in the high- to mid-frequency region is fitted by a model of interfacial charge transfer resistance R_{CT} and capacitance C_{dl} connected parallel to each other. The R_{CT} of CoZIF/CTAB drastically decreases from 384 Ω to approximately 4 Ω on CoCRD(600–800) electrodes. During electrosorption, R_{CT} is involved in the rate of ionic species charging within the capacitive structure [45]. This observation aligns with the effects of pyrolysis on the C_{dl} and ECSA properties.

Fig. 3g highlights the cycling performance of the CDI system in a 220 μS cm^{-1} NaCl solution under an applied bias of 1.2 V. Both CoZIF/CTAB and CoCRD(700) electrodes demonstrate consistent conductivity reduction and reversal over at least 7 runs. Nevertheless, the amplitude observed with the carbonized CoCRD(700) is larger compared to CoZIF/CTAB. Fig. S6 illustrates the desalination capacity of CoZIF/CTAB and CoCRD(700) electrodes, achieving 17.4 and 31.9 mg-NaCl g^{-1}, respectively (initial NaCl = 2 mM, applied bias = 1.2 V). Notably, CoCRD(700) outperforms reported carbon materials, such as AC (10.8 mg g^{-1}) [46], CNT (13.3 mg g^{-1}) [47], rGO (19.6 mg g^{-1}) [48], and ZIF-8 derived carbon (15 mg g^{-1}) [49], in the specific adsorption capacity (SAC) through CDI system. Fig. 3h shows the Ragone plots of carbon-based materials in the literature, illustrating the relationship between SAC and specific adsorption rate (SAR, mg min^{-1} g^{-1}). The data were compiled from experiments conducted with an initial 500 mg L^{-1} NaCl. MOF-derived electrodes exhibit relatively rapid deionization rates, with CoCRD(700) positioned in the uppermost right region, indicating its superior performance over other electrodes.

3.3. Batch electrosorption of Mo

Fig. 4a illustrates the effect of applied potential (vs. RHE, 10 mg-Mo L^{-1}, 3 mM $NaHCO_3$) on Mo electrosorption using the CoCRD(700) electrode in a CDI system, with corresponding chronoamperometry analysis shown in Fig. 4b. The initial drop in amperometric current in the first 5 min reflects the charging of ions into the electrode's capacitance. Following this, the anodic current stabilizes, and upon switching to 0 V, the current shifts in the cathodic direction, indicating ion release from the electrode surface. As summarized in Fig. 4c, the removal efficiency exceeds 85% within the potential range of +1.0 V - +1.2 V, achieving a maximum adsorption capacity of over 35 mg-Mo g^{-1}. Meanwhile, the molybdate removal is used to assess the charge efficiency (CE,%), which represents the equivalence of Mo removed relative to the integrated charges ($\int Idt$) under constant potential.

$$\mathrm{CE}(\%) = \frac{2F\Delta[Mo]V}{\int Idt} \times 100 \quad (3)$$

where F is the Faraday constant (96,485 coulomb mol^{-1}), V is the reaction volume (L), and $\Delta[Mo]$ is the Mo removed in molarity. A high CE of above 95% is achieved at a low electrode potential (+0.4 V), but decreases with increasing potential. Notably, CE remains approximately 50% at +0.8 − +1.2 V, where the adsorption capacity approaches its maximum. This trend predicts concurrent electron transfer associated with Co phase transformation at these potentials. Voltammetry analysis of the MOF electrodes reveals very weak redox currents upon the addition of molybdate ions, alongside the characteristic reversible peaks of Co oxides, as shown in Fig. S7. This finding implies that the electrode exhibits negligible activity toward Mo(VI) reduction, which is avoided

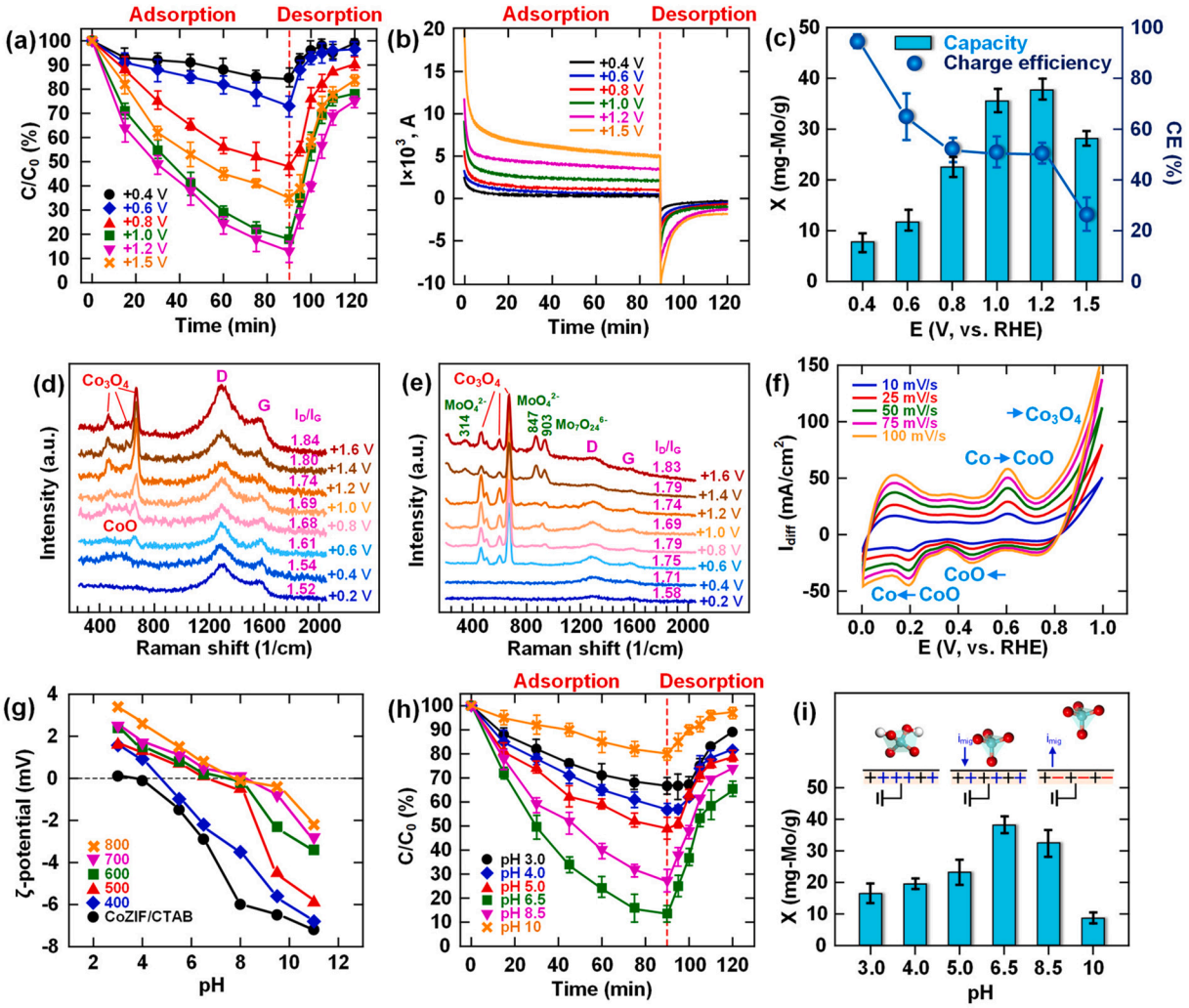

Fig. 4. Effects of electrode potential (vs. RHE) on (a) Mo electrosorption, with (b) corresponding chronoamperometry currents. (c) Mo adsorption capacity and charge efficiency of CoCRD(700) electrode as affected by working potentials (C0 = 10 mg-Mo L^{-1}, pH 8, 3 mM NaHCO3). Operando Raman spectra of CoCRD(700) (d) without and (e) with the addition of molybdate salt (100 mg-Mo L^{-1}, pH 8) at varied potentials (vs. RHE). (f) Diffusive current density of CoCRD(700) as a function of scan rate. (g) Zeta-potential analysis of MOF-derived carbons (0.1 M KCl). Effects of solution pH on (h) Mo electrosorption and (i) adsorption capacity using CoCRD(700) electrode.

by the presence of the cation exchange membrane. At +1.5 V the decline in Mo capacity and further reduction in CE (24%) can be attributed to the water splitting, particularly oxygen evolution.

The effects of molybdate salt addition on the surface species and phase transitions of Co in the CoCRD(700) electrode during anodic scanning are evaluated using operando Raman spectroscopy, as demonstrated in Fig. 4d and e. In the absence of Mo, the onset of CoO signals at +0.6 V is attributed to the anodization of Co oxide or hydroxide within the carbon framework [50]. As the potential increases to +1.0 V, progressive oxidation of CoO to Co_3O_4 is evident, based on appearance of Raman modes for E_g (463 cm^{-1}), F_{2g} (510/596 cm^{-1}), and A_{1g} (670 cm^{-1}) [51]. This transformation between CoO_x underscores the pseudocapacitive nature of Co-based electrodes [52]. Therefore, the pronounced increase in polarization at potentials of > +0.8 V, as shown in Fig. 4f, can thus be linked to the Co_3O_4 formation, with the diffusive current (I_{diff}) extracted from the total current of CoCRD(700) in Fig. 3b. In the presence of Mo, the intensity of Co_3O_4 peaks increases, suggesting the stabilization of this Co oxide phase. Concurrently, vibrational modes of MoO_4^{2-} at 314 and 847 cm^{-1}, and its condensed species $Mo_7O_{24}^{6-}$ at 903 cm^{-1} [53], become detectable at anodic potentials exceeding +0.8 V, confirming the adsorption and accumulation of Mo species under anode polarity. The transformation, governed by the Co^{2+}/Co^{3+} redox reaction (Eq. (4a)), catalytically supports interfacial charging/discharging processes. During this cycle, the charge imbalance arising from CoO-to-Co_3O_4 conversion is compensated by adsorbed MoO_4^{2-}, as described by Eq. (4b).

$$3C(Co^{2+}O) + H_2O \rightleftharpoons C(Co^{2+}Co_2^{3+}O_4) + 2e^- + 2H^+$$

$$C(Co^{2+}Co_2^{3+}O_4) + MoO_4^{2-} + 2H^+ \longrightarrow 3C(Co^{2+}O)^{2+}(MoO_4^{2-}) + H_2O \quad \text{(4a and 4b)}$$

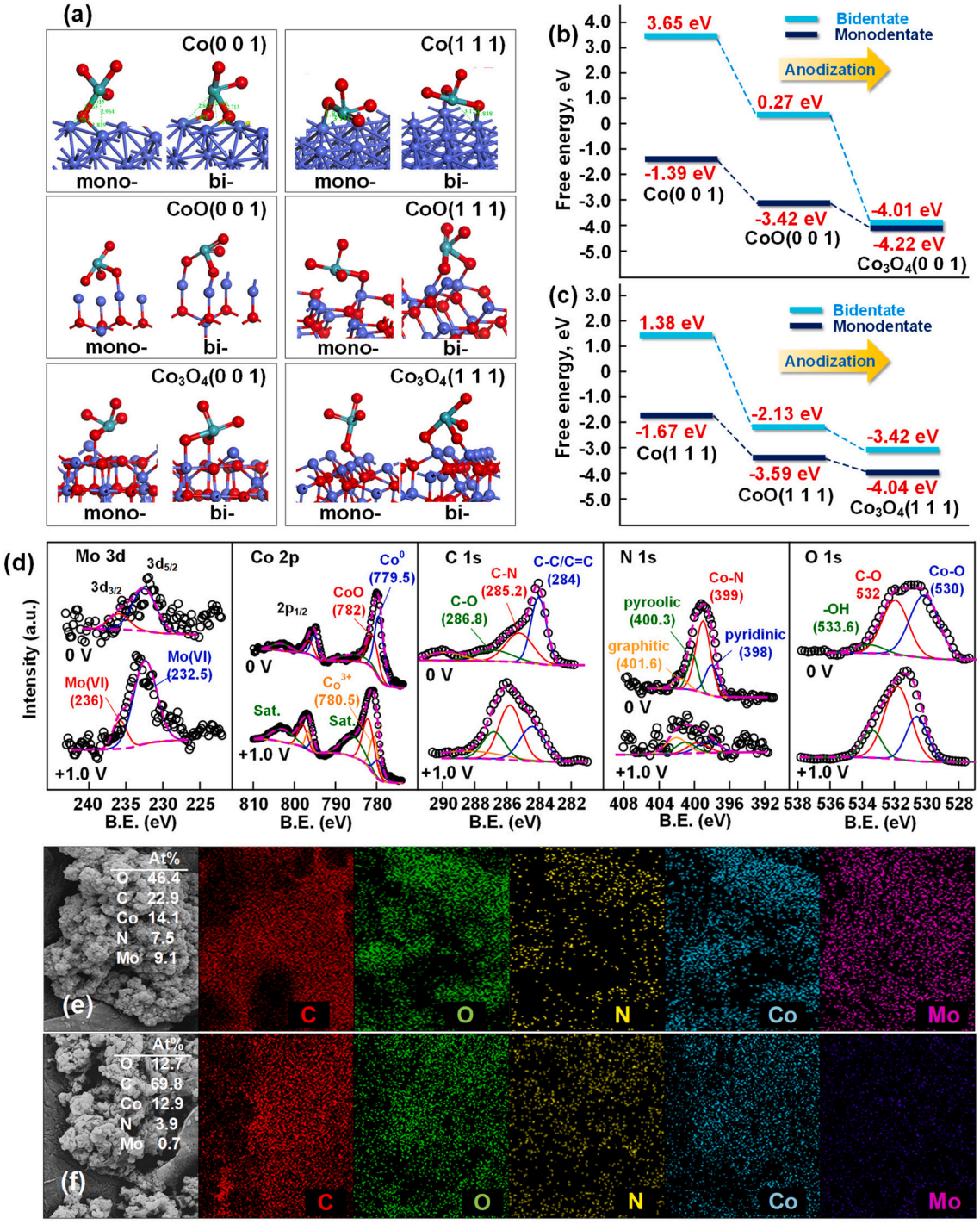

Fig. 5. (a) DFT simulation of molybdate adsorption on Co, CoO, and Co3O4 sites in monodentate and bidentate configurations, with corresponding adsorption energies on (b) (0 0 1) and (c) (1 1 1) facets. (d) XPS, and elemental mapping of CoCRD(700) electrode for (e) Mo electrosorption at +1.0 V, and (f) desorption at 0 V.

Additionally, the increasing I_D/I_G ratio in carbon bands with elevated potentials indicates relaxation of graphitic carbon lattice [54], thereby enhancing the structural disorder of the CRD framework.

It is expected that the surface acidity is a critical factor determining the charged nature of functional groups on materials. The pH-responsive surfaces, which override the positive electrode polarity, are likely responsible for the asymmetry sorption for anions and cations [55]. As displayed in Fig. 4g, the zeta-potential of the MOF-derived electrodes (ionic strength = 0.1 M KCl) indicates a shift in the point of zero charge (pH_{PZC}). The pH_{PZC} of CoZIF/CTAB is 4, increasing to around pH 8 with higher pyrolysis temperatures. The negative surface charge of ZIF may originate from the pK_a of 4–6 for imidazole and its derivatives [56]. In contrast, the pH_{pzc} of cobalt oxides, such as CoO, Co_3O_4, and CoOOH, typically falls within the range of 7–9 [57]. Therefore, as Co^{2+} ions chelated in the organic ligands are converted to oxides upon pyrolysis, the CoO sites embedded in the carbon matrix reduce overall surface negativity of CoCRD. Fig. 4h demonstrates Mo electrosorption at a working potential of +1.0 V at various controlled pH in the range of 3–10. The controlled pH strongly influences Mo removal, which is maximized at pH 6.5, as depicted in Fig. 4i. The adsorption capacity optimized by pH can be explained by the mass transport mechanism. Based on the acidic constants of molybdate, non-charged H_2MoO_4 predominates at pH below 3.5, dissociating into charged $HMoO_4^-$ and MoO_4^{2-} at pH >3.5 (Fig. S1). Mo is anticipated to be electrostatically removed when pH increases, while ignoring the multinuclear species at pH lower than 2. When the observed EDL capacitance (C_{dl}) is resulted from two surfaces in parallel, the polarizable C_E and the pH-reversible C_{pH} [58],

$$C_{dl} = \frac{d\sigma_0^E}{d\varnothing} + \frac{d\sigma_0^{pH}}{d\varnothing} = \frac{d\sigma_0^E}{d\varnothing} + \frac{d\sigma_0^E}{dpH}\frac{dpH}{d\varnothing} = \frac{d\sigma_0^E}{d\varnothing} - 16.9\frac{d\sigma_0^E}{dpH} = C_E + C_{pH} \quad (5)$$

the sign of migration current (I_{mig}) for Mo oxyanions reverses as pH-responsive function groups are converted from positive to negative [59]. Zeta-potential analysis has indicated a pH_{pzc} of 8 for CoCRD (Fig. 4g). Thus, even under anodic potential, the surface negativity at pH 8.5–10 will interfere the removal of negatively charged Mo species, and reduce adsorption capacity.

To further investigate the effect of Co transformation on the bonding mode of molybdate molecule, density function theory (DFT) calculations are used to formulate the energy state changes. Detailed methods and parameters are provided in the Supporting Information S4. Surface functional groups are supposed to coordinate with Co atoms in the solid phase, forming inner-sphere complexes with non-protonated MoO_4^{2-} in either bidentate or monodentate ligands [60,61]. Fig. 5a depicts the results of geometry optimization, where the free energy of molybdate on

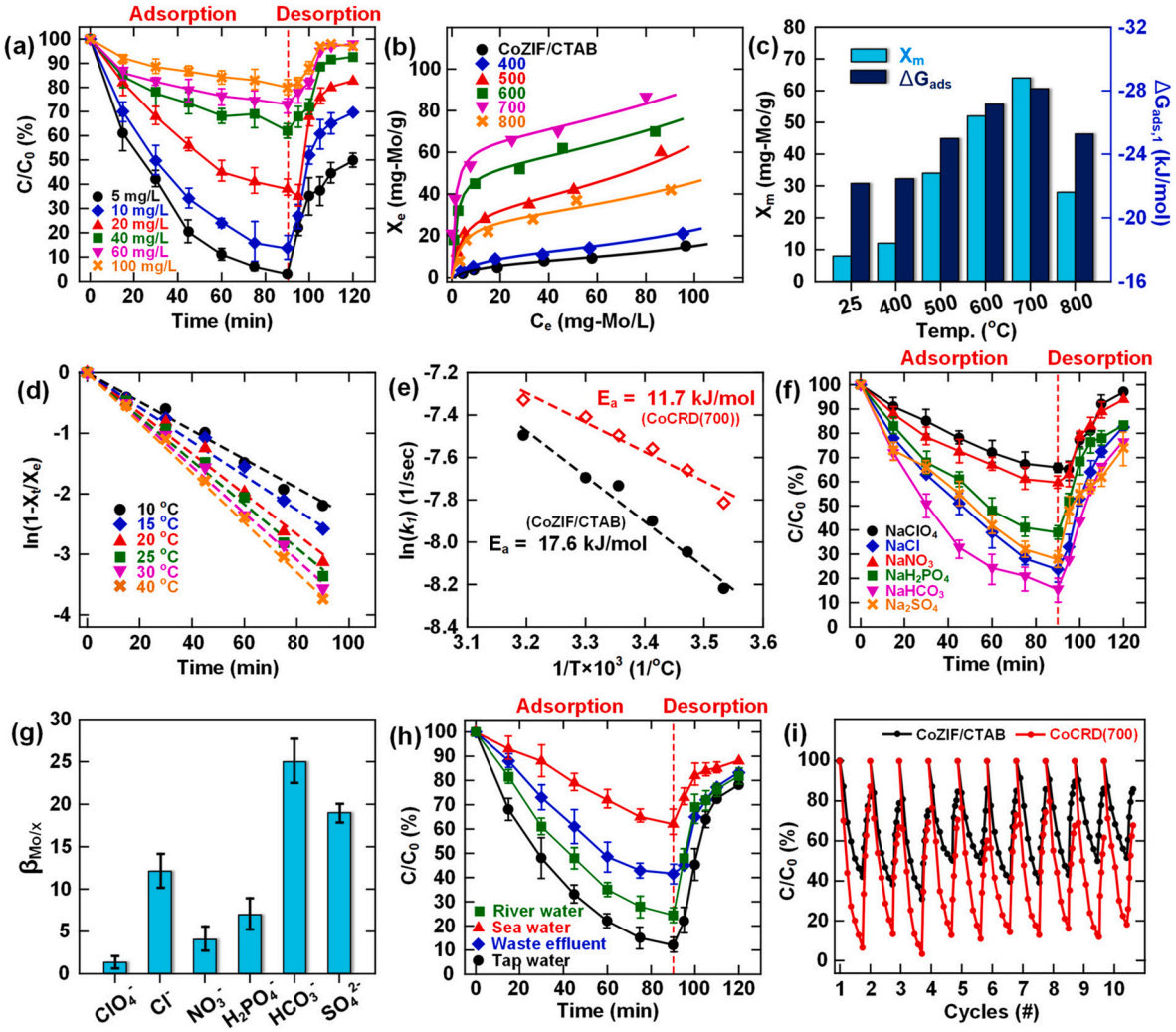

Fig. 6. (a) Effect of initial Mo concentration on Mo electrosorption using CoCRD(700) electrodes. (b) Mo adsorption isotherms, and corresponding (c) monolayer capacities and adsorption free energies of the CoZIF/CTAB-derived electrodes (3 mM NaHCO3, pH 8, E = +1.0 V vs. RHE). (d) First-order rate fitting for Mo electrosorption at different temperatures and (e) activation energies based on Arrhenius equation. Effects of electrolyte type on (f) Mo electrosorption and (g) selectivity factors. (h) Electrosorption in different real water samples using CoCRD(700) electrode (C0 = 10 mg-Mo L^{-1}) and (i) cycling performance for Mo removal.

Co surfaces follows Eq. (6):

$$E_{ads} = E_{Co(hkl)-Mo} - E_{Co(hkl)} - nE_{MoO_4^{2-}} \quad (6)$$

$E_{Co(hkl)-Mo}$ and $E_{Co(hkl)}$ represent total energies of the Co surface before and after Mo adsorption. The Gibbs free energies for MoO_4^{2-} on two primary facets, Co(0 0 1) and Co(1 1 1), are illustrated in Fig. 5b and c, respectively. Consequently, the adsorption energy is relatively low as molybdate adopts a monodentate on metallic Co. At low electrode potentials, Mo adsorption, particularly in the case of bidentate, is endothermic on both Co(0 0 1) and Co(1 1 1) surfaces with positive adsorption energy. With elevating the potentials, the energies become exothermic when Co undergoes recrystallization into CoO and Co_3O_4, indicating a more stable adsorption interaction. The bidentate species results in a greater accumulation of negative charge at the surface compared to the monodentate one. For instance, in the Co—O coordination shell on Co(0 0 1), Co atoms are surrounded by O atoms at approximately 1.83 Å, while in the Co—Mo coordination shell, the atomic distance reduces from 3 Å in monodentate to 2.6 Å in bidentate (Fig. S8). In this arrangement, the monodentate species, which keeps most of its negative charge away from the surface, is energetically preferred [62]. This computation suggests that Mo adsorption can be stabilized upon anodization, attributed not only to simple electrostatic attraction in the EDL but only to surface complexation at oxide-water interfaces. Fig. 5d presents the chemical state changes in CoCRD(700) after Mo electrosorption at +1.0 V and subsequent desorption at 0 V. Compared to the fresh electrode, an additional Mo binding energy is observed on the used CoCRD(700), evidenced by the Mo(VI) $3d_{5/2}$ and $3d_{3/2}$ peaks at 232.5 and 236 eV, respectively [63]. The weakening of Mo signals after desorption suggests effective Mo release from the electrode surface through polarity reversal. Meanwhile, the emergence of Co^{3+} state (780.5 eV for $2p_{3/2}$ orbital) and its shake-up satellite peak during electrosorption corresponds to the formation of the Co_3O_4 phase [64], which disappears after desorption. This modification confirms the reversibility of CoO-to-Co_3O_4 redox reactions. Additionally, decreased C—O intensities in the C 1s and O 1s spectra, along with intensified Co—N in the N 1s spectrum, also indicate the structural alterations in CoCRD(700) under different potentials. The elemental mappings of CoCRD after Mo electrosorption at +1.0 V and subsequent desorption at 0 V are provided in Fig. 5e and f, respectively. Following adsorption, the atomic percentages of O and Mo reach 46% and 9%, respectively, then decrease to 12.7% and 0.7% after desorption. The simultaneous rise and decline of both O and Mo signals indicate the restoration of surface sites by potential switching in a range of Co and Co_3O_4 formation.

Mo electrosorption on CoCRD(700) is operated at molybdate concentrations C_0 ranging from 5 to 100 mg-Mo L^{-1}, as shown in Fig. 6a. Preliminary tests have shown that Mo concentration profiles approached plateaus during the adsorption and desorption phases within 90 and 30 min, respectively, as shown in Fig. S9a. Thermodynamically, the residual Mo on the electrode surface is expected to reach equilibrium with molybdate ions in solution at constant potentials. On the other hand, at a fixed electrode area, while lowing the initial Mo concentration leads to high removal efficiency (C/C_0), a corresponding decline in desorption efficiency is observed. Since Mo desorption is carried out by reversing the polarity to 0 V, the repulsion between the electrode surface and Mo anions is weaker than the attraction exerted during adsorption at +1.2 V. As depicted in Fig. S9b, the Mo capacities – calculated from removal data in Fig. 6a – converge to similar levels across various initial concentrations. The fractional contribution of residual Mo becomes more pronounced at lower initial concentrations, thereby reducing the apparent desorption efficiency. The Mo adsorption capacity (X_e, mg g^{-1}) is estimated at 90 min under conditions: constant potential = +1.0 V (vs. RHE), 298 K, and pH 6.5.

$$X_e = \frac{C_0 - C_{90}}{m} \times V \quad (7)$$

where m is the mass (g) of the synthesized MOF-derived material coated onto the graphite substrate and C_{90} is the concentration at 90 min. Fig. 6b provides Mo adsorption isotherms on the CoCRD electrodes, which are difficult to fit using a simple monolayer model. Given the heterogeneity of porous structure, it is inferred that the adsorption energy varies as Mo oxyanions are captured in different forms. Since Mo heteropolyanions were identified in Raman spectra at elevated potentials, a type-II model should better describes their electrosorption mechanism [65]:

$$X_e = \frac{K_1 C_{90}(X_m)}{(1 - K_2 C_{90})(1 + (K_1 - K_2)C_{90})} \quad (8)$$

where K_1 and K_2 represent adsorption constants for the monolayer and subsequent layers (L mg^{-1}), respectively, and X_m denotes the monolayer capacity. Notably, when K_2 is insignificant, Eq. (8) simplifies to the Langmuir model, corresponding to a type-I isotherm. Fig. 6c compiles X_m values of CoCRD electrodes, alongside the corresponding adsorption energy (ΔG_{ads}) obtained from the monolayer constant K_1 ($\Delta G_{ads,1} = -2.303RTlogK_1$, where K_1 is expressed in a unit of L mol^{-1}). The adsorption capacity (X_m) for Mo oxyanions increases from 8 mg-Mo g^{-1} for CoZIF/CTAB to 64 mg-Mo g^{-1} for CoCRD(700). The monolayer energy ($\Delta G_{ads,1}$) of −22 kJ mol^{-1} on CoZIF/CTAB also increases to −28 kJ mol^{-1} on CoCRD(700), suggesting the impact of carbonization on the bonding strength for Mo species. The improvement in adsorption capacity with pyrolysis temperature is rationally attributed to the expended effective surface area provided by Co-enriched carbon surfaces. As displayed in Fig. S9c, the CoCRD capacity for molybdate ions exhibited a strong correlation with the average pore size (as determined by BET analysis). In CDI studies, it is widely accepted that micropores in activated carbons serve as adsorption sites, while mesopores lower ion transportation resistance into the electrode material [66]. An optimal pore size distribution therefore benefits both electrosorption rate and overall capacity. The appearance of Mo singles, coinciding with the

Table 1
Summary of adsorbents used for Mo removal.

Adsorbent	Materials	Conditions	Properties	Ref.
AlEG-Pro(1)-700	γ-AlOOH	1000 mg L^{-1}, pH 3	X_m = 41 mg-Mo g^{-1}	67
s-$Al_{24}T_{70}$	γ-Al_2O_3	100 mg L^{-1}, pH 3	X_m = 56 mg-Mo g^{-1}	68
Alumina	α-Al_2O_3	1000 mg L^{-1}, pH 4	X_m = 33 mg-Mo g^{-1}	69
Montmorillonite	Aluminosilicate	50 mg L^{-1}, pH 6.5	X_m = 7 mg-Mo g^{-1}	11
Zeolite 4A	Aluminosilicate	150 mg L^{-1}, pH 1	X_m = 3.5 mg-Mo g^{-1}	70
IOCS	Iron oxide-SiO_2	100 mg L^{-1}, pH 4	X_m = 2 mg-Mo g^{-1}	71
$SiO_2Fe_xO_y$	Iron oxide-SiO_2	100 mg L^{-1}, pH 8	X_m = 11 mg-Mo g^{-1}	72
Maghemite	γ-Fe_2O_3	100 mg L^{-1}, pH 5	X_m = 33 mg-Mo g^{-1}	73
Pyrite	FeS_2	10 mg L^{-1}, pH 4	X_m = 5 mg-Mo g^{-1}	74
Mo(VI)-MIIP	Fe_3O_4@SiO_2	100 mg L^{-1}, pH 1	X_m = 31 mg-Mo g^{-1}	75
ZSM	Fe_3O_4/zeolite	25 mg L^{-1}, pH 3	X_m = 18 mg-Mo g^{-1}	76
Chromium ferrite	$CrFe_2O_4$	100 mg L^{-1}, pH 3	X_m = 30 mg-Mo g^{-1}	77
MWCNT(NaOCl)	Carbon nanotube	10 mg L^{-1}, pH 7	X_m = 22.7 mg-Mo g^{-1}	78
CDC	Carbide	10 mg L^{-1}, pH 3–5	X_m = 16 mg-Mo g^{-1}	12
Electrosorption CoCRD(700)	CoO/Carbon	100 mg L^{-1}, pH 6.5	X_m = 87 mg-Mo g^{-1}	This work

transformation of Co oxide phase in in-situ Raman spectra, indicates the predominant role of Co sites in Mo adsorption. Therefore, the well-dispersed cobalt in the composite, together with appropriate pore structure, creates a synergistic effect specifically on Mo capacity. While the Co crystallites embedded in CRD grows at higher temperatures, the X_m decreases to 28 mg-Mo g^{-1} on CoCRD(800). Additionally, the multilayer energy ($\Delta G_{ads,2}$) averages −15 kJ mol^{-1} for MOF-derived electrodes, but slightly decreases to −14 kJ mol^{-1} for CoCRD(700), as listed in Table S3. This finding indicates that Mo species are preferentially adsorbed onto the monolayer, with weaker interactions observed in subsequent layers.

To the best of our knowledge, there are currently no journal research specifically addressing Mo removal through electrosorption. Due to the negatively charged nature of polynuclear Mo complexes, acidic electrolyte (pH 3) are often required to enhance the adsorbent capacity. Metal oxides, which typically have neutral pH_{pzc} values, have also demonstrated effectiveness for divalent MoO_4^{2-} at pH around 7, especially at low concentrations (10–100 mg-Mo g^{-1}). As summarized in Table 1, among adsorbents for Mo, Al and Fe minerals are the most prevalent. Aluminum oxides, such as boehmite [67], gibbsite [68,69], aluminosilicate, such as montmorillonite [11] and zeolite [70], and iron oxides, such as ferrihydrite [71,72], hematite [73], pyrite [74], magnetite [75,76], and spinel ferrite [77], exhibit specific surface characteristics that are suited for Mo adsorption. Carbon-based materials like MWCNT [78] and carbon carbide [12] are also employed for Mo adsorption due to their relatively larger surface area compared to metal oxides. This study is the first to utilize a CDI system for recovering Mo through charging/discharging processes. The *Co*-enriched carbon polyhedrons demonstrate a high adsorption capacity for Mo oxyanions, which can be attributed to the increased surface positivity facilitated by the redox transition from CoO to Co_3O_4 during anodization. As a result, electrosorption using CoCRD(700) offers a more effective way, featuring higher capacity for Mo at neutral pH and rapid regeneration via polarity reversal, compared to the conventional adsorption.

Mo electrosorption at different temperatures is evaluated to analyze the chemical kinetics, as shown in Fig. S10. The adsorption capacities of CoZIF/CTAB and CoCRD(700) for molybdate oxyanions are measured at +1.0 V (vs. RHE) and an initial Mo level of 10 mg L^{-1}. As the adsorption reaches equilibrium in 90 min, a pseudo first-order rate model is applied to obtain the rate constant k_1, as described below:

$$-\frac{dC_{Mo}}{dt} = k_1(C_t - C_{90}) \tag{9a}$$

$$\ln\left(\frac{C_t - C_{90}}{C_0 - C_{90}}\right) = -k_1 t \tag{9b}$$

$$\ln\left(1 - \frac{X_t}{X_e}\right) = -k_1 t \tag{9c}$$

Fig. 6d presents the linear correlation of CoCRD(700) capacity as a function of $\ln(1 - X_t/X_e)$ versus t, where the slope denotes the rate constant (k_1, in unit of sec^{-1}). Activation energy (E_a, kJ mol^{-1}) is estimated by plotting $\ln(k_1)$ against the reciprocal temperature (1/T), based on the Arrhenius equation:

$$\ln(k_1) = \ln A - \frac{E_a}{R}\left(\frac{1}{T}\right) \tag{10}$$

where A is the collision frequency constant. As displayed in Fig. 6e, E_a values of CoZIF/CTAB and CoCRD(700) are 17.6 and 11.7 kJ mol^{-1}, respectively. The activation involves the rate-limiting step of physicochemical reactions. While E_a falls within the range of 5 to 40 kJ mol^{-1}, the mass transport mechanism predominates the chemical process. This result indicates that the Mo removal rate is significantly dependent on the ion diffusion on both the MOF-derived electrodes. The lower activation for CoCRD(700) is attributed to its enhanced mesoporosity, as well as surface positivity induced by in-situ recrystallized Co nanoparticles embedded in the carbon polyhedrons. These features collectively accelerate Mo diffusion and immobilization.

Fig. 6f demonstrates Mo removal in the presence of various sodium salts (x = 3 mM, with a molar concentration ratio of *x* to Mo approximately 30). This selectivity for Mo oxyanions relative to competitive ions can be quantified by the separation factor, β, defined as [81]:

$$\beta_{Mo/x} = \left(\frac{C_{Mo,0} - C_{Mo,90}}{C_{x,0} - C_{x,90}}\right) \times \left(\frac{C_{x,0}}{C_{Mo,0}}\right) \tag{11}$$

where $C_{x,0}$ and $C_{x,90}$ denote the initial and 90-min concentrations of the competitive anion *x*, respectively. As illustrated in Fig. 6g, the $\beta_{Mo/x}$ factor are all greater than one, confirming the high affinity of CoCRD for molybdate ions. High selectivity factors for common surface water ions – such as alkalinity ($\beta_{Mo/HCO_3^-} = 25$), sulfate ($\beta_{Mo/SO_4^{2-}} = 19$), and chloride ($\beta_{Mo/Cl^-} = 12$) – suggest their minimal interference in Mo electrosorption. In contrast, ClO_4^- and NO_3^- are the two most competitive species. The adsorption selectivity is governed by the strength of electrostatic interactions between ionic species and the adsorbent's active sites, which depends on both ionic valence and effective size. The ratio of hydrated radius to crystal radius for the studied anions follows the order: HCO_3^- (1.97) > Cl^- (1.83) > SO_4^{2-} (1.39) > $H_2PO_4^-$ (1.27) > NO_3^- (1.26) > MoO_4^{2-} (1.19) > ClO_4^- (1.16) [79,80]. This sequence well predicts the impact of co-existing anions on Mo electrosorption, with multivalent ions typically dominating over smaller, highly hydrated monovalent ions. Since molybdenum existed as molybdate oxyanions, the relative selectivity was examined among various anions. Mo removal can be solely ascribed to anode-side adsorption, as the CDI cell was separated by a cation exchange membrane, preventing cathode reduction of Mo species. The effects of the water matrix on Mo electrosorption (C_0 = 10 mg L^{-1}) are presented in Fig. 6h. Table S4 provides the compositions of river water, effluent from a wastewater treatment plant, and seawater, with corresponding ionic strengths of 9.56×10^{-3}, 0.0125, and 0.64 eq. L^{-1}, respectively. Compared to the Mo adsorption capacity of CoCRD electrode in tap water (39.8 mg-Mo L^{-1}), the capacity decreases but remains acceptable in river water (34.2 mg-Mo L^{-1}) and waste effluent (31 mg-Mo L^{-1}). However, a significant decline in the capacity is observed in seawater (12 mg-Mo L^{-1}), due to the extremely high salinity. Additionally, natural organic matters in real waters, typically present at around 10 ppm-COD, may compete with molybdate ions – particularly when associated with carboxylic acid functional groups. However, in the Mo electrosorption experiments, the potential impact of COD was difficult to assess, as the fresh and used CoCRD electrodes were minimal, according to EDS mapping results. The durability of the MOF-derived electrodes was assessed through repeated electro-sorption and desorption cycles. Each cycle consisted of a 90-min adsorption phase at +1.0 V, followed by 30-min desorption phase at 0 V in a 10 mg-Mo L^{-1} solution. As shown in Fig. 6i, both CoZIF/CTAB and CoCRD(700) achieve Mo removal efficiencies exceeding 60% and 95%, respectively, during the first three cycles. A gradual decline in Mo uptake is observed over subsequent cycles, likely due to incomplete desorption from the previous run. Nonetheless, both electrodes maintain steady performance for at least 10 cycles, revealing their stability and reproducibility.

4. Conclusions

Mesoporous *Co*-enriched carbon polyhedrons, CoCRD, were synthesized for molybdate electrosorption using a cobalt imidazolate precursor, CoZIF/CTAB. Through solvothermal treatment followed by pyrolysis, Co^{2+} nodes recrystallized into CoO/Co nanoparticles and nanoclusters embedded within carbon skeleton. This carbonization enhanced the EDL capacitance and increased effective surface area for Mo immobilization. The pseudocapacitance characteristics of CoCRD originated from reversible Co redox reactions, where Co sites

contributed to pH-responsive functional groups and surface positivity, facilitating the adsorption of oxyanions under neutral pH conditions. Operando Raman spectroscopy and DFT calculations confirmed that the catalytic transformation of CoO to Co_3O_4 in the carbon framework, driven by increasing the anodic potential, promoted molybdate electrosorption in a monodantete complex. The maximum adsorption capacity of CoCRD(700) reached 87 mg-Mo g^{-1} at +1.0 V (vs. RHE) and pH 6.5. A low activation energy (~12 kJ mol^{-1}) and high selectivity for MoO_4^{2-} anions indicated the viability of Mo recovery, which could be achieved by simply reversing the polarity of the CoCRD(700) electrode in a membrane capacitive deionization system.

CRediT authorship contribution statement

Yu-Jen Shih: Writing – review & editing, Writing – original draft, Visualization, Validation, Supervision, Resources, Project administration, Methodology, Investigation, Funding acquisition, Conceptualization. **Zhi-Lun Wu:** Software, Methodology, Formal analysis, Data curation. **Ming-Rui Wang:** Validation, Methodology, Investigation, Formal analysis, Data curation. **Chin-Pao Huang:** Conceptualization, Investigation, Methodology, Supervision.

Declaration of competing interest

The authors declare that they have no known competing financial interests or personal relationships that could have appeared to influence the work reported in this paper.

Acknowledgement

The National Science and Technology Council, Taiwan, is appreciated for generous finance support of this research project under Contract No. NSTC 111-2221-E-110-007-MY3.

Appendix A. Supplementary data

Supplementary data to this article can be found online at https://doi.org/10.1016/j.cej.2025.164426.

Data availability

Data will be made available on request.

References

[1] K.S. Tsai, Y.M. Chang, C.M. Kao, K.L. Lin, Groundwater molybdenum from emerging industries in Taiwan, Bull. Environ. Contam. Toxicol. 96 (2016) 102–106, https://doi.org/10.1007/s00128-015-1695-1.
[2] T. Pichler, S. Koopmann, Should monitoring of molybdenum (Mo) in groundwater, drinking water and well permitting made mandatory? Environ. Sci. Technol. 54 (2020) 1–2, https://doi.org/10.1021/acs.est.9b06869.
[3] C.W. Wang, C. Liang, H.J. Yeh, Aquatic acute toxicity assessments of molybdenum (+VI) to Daphnia magna, Chemosphere 147 (2016) 82–87, https://doi.org/10.1016/j.chemosphere.2015.12.052.
[4] P.L. Smedley, D.M. Cooper, D.J. Lapworth, Molybdenum distributions and variability in drinking water from England and Wales, Environ. Monit. Assess. 186 (2014) 6403–6416, https://doi.org/10.1007/s10661-014-3863-x.
[5] T.H. Nguyen, M.S. Lee, Recovery of molybdenum and vanadium with high purity from sulfuric acid leach solution of spent hydrodesulfurization catalysts by ion exchange, Hydrometallurgy 147–148 (2014) 142–147, https://doi.org/10.1016/j.hydromet.2014.05.010.
[6] R. Kumar, C. Liu, G.S. Ha, K.H. Kim, S. Chakrabortty, S.K. Tripathy, Y.K. Park, M. A. Khan, K.K. Yadav, M.M.S. Cabral-Pinto, B.H. Jeon, A novel membrane-integrated sustainable technology for downstream recovery of molybdenum from industrial wastewater, Resour. Conserv. Recycl. 196 (2023) 107035, https://doi.org/10.1016/j.resconrec.2023.107035.
[7] J.J. Cruywagen, A.G. Draaijer, J.B.B. Heyns, E.A. Rohwer, Molybdenum(VI) equilibria in different ionic media. Formation constants and thermodynamic quantities, Inorg. Chim. Acta 331 (2002) 322–329, https://doi.org/10.1016/S0020-1693(02)00700-4.
[8] W. Ma, X. Sha, L. Gao, Z. Cheng, F. Meng, J. Cai, D. Tan, R. Wang, Effect of iron oxide nanocluster on enhanced removal of molybdate from surface water and pilot scale test, Coll. Surf. A: Physicochem. Eng. Asp. 478 (2015) 45–53, https://doi.org/10.1016/j.colsurfa.2015.03.032.
[9] M. Kersten, Temperature-dependent adsorption by goethite of molybdate and vanadate, Appl. Geochem. 162 (2024) 105907, https://doi.org/10.1016/j.apgeochem.2024.105907.
[10] B. Muir, D. Andrunik, J. Hyla, T. Bajda, The removal of molybdates and tungstates from aqueous solution by organo-smectites, Appl. Clay Sc. 136 (2017) 8–17, https://doi.org/10.1016/j.clay.2016.11.006.
[11] I. Ali, T. Kon'kova, A. Rysev, Z.A. ALothman, M. Sillanpää, J. Georgin, X. Y. Mbianda, Removal of dichromate-, molybdate-, and nitrate ions from wastewater using modified natural montmorillonite, J. Mol. Liq. 392 (2023) 123400, https://doi.org/10.1016/j.molliq.2023.123400.
[12] Y. Manawi, S. Simson, J. Lawler, V. Kochkodan, Removal of molybdenum from contaminated groundwater using carbide-derived carbon, Water 15 (1) (2023) 49, https://doi.org/10.3390/w15010049.
[13] A.Y. Ahmad, M.A. Al-Ghouti, M. Khraisheh, N. Zouari, Insights into the removal of lithium and molybdenum from groundwater by adsorption onto activated carbon, bentonite, roasted date pits, and modified-roasted date pits, Biore. Technol. Rep. 18 (2022) 101045, https://doi.org/10.1016/j.biteb.2022.101045.
[14] F.A. Bertoni, J.C. González, S.I. García, L.F. Sala, S.E. Bellú, Application of chitosan in removal of molybdate ions from contaminated water and groundwater, Carbohydr. Polym. 180 (2018) 55–62, https://doi.org/10.1016/j.carbpol.2017.10.027.
[15] M.S. Gaikwad, S.K. Suman, K. Shukla, A.V. Sonawane, S.N. Jain, A review on recent contributions in the progress of membrane capacitive deionization for desalination and wastewater treatment, Int. J. Environ. Sci. Technol. 20 (2023) 14073–14088, https://doi.org/10.1007/s13762-023-04778-z.
[16] K. Dybowski, G. Romaniak, P. Kula, A. Sobczyk-Guzenda, B. Januszewicz, A. Jędrzejczak, Ł. Kaczmarek, B. Burnat, P. Krzyczmonik, T. Kaźmierczak, J. Siniarski, Composite carbon electrode with a coating of nanostructured, reduced graphene oxide for water electrodialysis, J. Appl. Electrochem. (2024), https://doi.org/10.1007/s10800-024-02157-1.
[17] S. Porada, L. Weinstein, R. Dash, A. van der Wal, M. Bryjak, Y. Gogotsi, P. M. Biesheuvel, Water desalination using capacitive deionization with microporous carbon electrodes, ACS Appl. Mater. Interfaces 4 (2012) 1194–1199, https://doi.org/10.1021/am201683j.
[18] M. Kim, X. Xu, R. Xin, J. Earnshaw, A. Ashok, J. Kim, T. Park, A.K. Nanjundan, W. A. El-Said, J.W. Yi, J. Na, Y. Yamauchi, KOH-activated hollow ZIF-8 derived porous carbon: Nanoarchitectured control for upgraded capacitive deionization and supercapacitor, ACS Appl. Mater. Interfaces 13 (2021) 52034–52043, https://doi.org/10.1021/acsami.1c09107.
[19] N. Pugazhenthiran, S.S. Gupta, A. Prabhath, M. Manikandan, J.R. Swathy, V. K. Raman, T. Pradeep, Cellulose derived Graphenic fibers for capacitive desalination of brackish water, ACS Appl. Mater. Interf. 7 (2015) 20156–20163, https://doi.org/10.1021/acsami.5b05510.
[20] S. Fleischmann, J.B. Mitchell, R. Wang, C. Zhan, D. Jiang, V. Presser, V. Augustyn, Pseudocapacitance: from fundamental understanding to high power energy storage materials, Chem. Rev. 120 (2020) 14, https://doi.org/10.1021/acs.chemrev.0c00170.
[21] A.R. Finney, I.J. McPherson, P.R. Unwin, M. Salvalaglio, Electrochemistry, ion adsorption and dynamics in the double layer: a study of NaCl(aq) on graphite, Chem. Sci. 12 (2021) 11166–11180, https://doi.org/10.1039/D1SC02289J.
[22] M. Kim, K.K. Leong, N. Amiralian, Y. Bando, T. Ahamad, S.M. Alshehri, Y. Yamauchi, Nanoarchitectured MOF-derived porous carbons: road to future carbon materials, Appl. Phys. Rev. 11 (2024) 041317, https://doi.org/10.1063/5.0213150.
[23] Y.J. Shih, S.K. Lin, Z.L. Wu, W.H. Chen, Cobalt and zinc imidazolate encapsulated in reduced graphene oxide and the derived nitrogen-enriched carbon frameworks (CoNC@rGO) for electrochemically sensing acetaminophen (APAP), Chem. Eng. J. 481 (2024) 148437, https://doi.org/10.1016/j.cej.2023.148437.
[24] R.N. Dürr, E. Stéphan, J. Leroy, F. Oswald, B. Verhaeghe, B. Jousselme, Efficient, stable, and solvent-free synthesized single-atom catalysts: carbonized transition metal-doped ZIF-8 for the hydrogen evolution reaction, ChemElectroChem 10 (2023) e202300205, https://doi.org/10.1002/celc.202300205.
[25] M.B. Gawande, P. Fornasiero, R. Zbořil, Carbon-based single-atom catalysts for advanced applications, ACS Catal. 10 (2020) 2231–2259, https://doi.org/10.1021/acscatal.9b04217.
[26] E. Asadi, A. Ghadimi, S.S. Hosseini, B. Sadatnia, M. Rostamizadeh, A. Nadeali, Surfactant-mediated and wet-impregnation approaches for modification of ZIF-8 nanocrystals: mixed matrix membranes for CO_2/CH_4 separation, Microp. Mesop. Mater. 329 (2022) 111539, https://doi.org/10.1016/j.micromeso.2021.111539.
[27] J.W. Park, P. Sivakumar, J. Lee, H. Jung, Well-dispersed cobalt magnetic nanoparticles incorporated into 3D mesoporous graphene, J. Porous. Mater. 30 (2023) 2079–2086, https://doi.org/10.1007/s10934-023-01490-8.
[28] P.S. Tseng, L.X. Chang, Y.S. Ou, C.M. Chou, C.S. Tsao, Y. Wu, J.P. Chou, P.J. Chen, C.Y. Wang, ZIF-67 derived co nanoparticles on ZIF-derived carbon for hydrogen spillover and storage, Appl. Surf. Sc. 638 (2023) 158097, https://doi.org/10.1016/j.apsusc.2023.158097.
[29] B. Ilkiv, S. Petrovska, R. Sergiienko, O. Foya, O. Ilkiv, E. Shibata, T. Nakamura, Y. Zaulychnyy, Electronic structure of hollow graphitic carbon nanoparticles fabricated from acetylene carbon black, Full. Nanotub. Carbon Nanostr. 23 (5) (2014) 449–454, https://doi.org/10.1080/1536383X.2014.885957.
[30] M.A. Ehsan, A.S. Hakeem, A. Rehman, Hierarchical growth of CoO nanoflower thin films influencing the electrocatalytic oxygen evolution reaction, Electrocatalysis 11 (2020) 282–291, https://doi.org/10.1007/s12678-020-00585-z.

[31] M. Farrag, G.A.M. Ali, Hydrogen generation of single alloy Pd/Pt quantum dots over Co3O4 nanoparticles via the hydrolysis of sodium borohydride at room temperature, Sci. Rep. 12 (2022) 17040, https://doi.org/10.1038/s41598-022-21064-z.
[32] Y. Li, J. Kim, J. Wang, N.L. Liu, Y. Bando, A.A. Alshehri, Y. Yamauchi, C.H. Hou, Kevin C.W. Wu, High performance capacitive deionization using modified ZIF-8-derived, N-doped porous carbon with improved conductivity, Nanoscale 10 (2018) 14852–14859, https://doi.org/10.1039/C8NR02288G.
[33] M. Kim, H. Nara, Y. Asakura, T. Hamada, P. Yan, J. Earnshaw, M. An, M. Eguchi, Y. Yamauchi, End-to-end pierced carbon Nanosheets with Meso-holes, Adv. Sci. 12 (2025) 2409546, https://doi.org/10.1002/advs.202409546.
[34] B. Rivas-Murias, V. Salgueiriño, Thermodynamic CoO–Co3O4 crossover using Raman spectroscopy in magnetic octahedronshaped nanocrystals, J. Raman Spectrosc. 48 (2017) 837–841, https://doi.org/10.1002/jrs.5129.
[35] O. Abuzalat, H. Tantawy, M. Basuni, M.H. Alkordi, A. Baraka, Designing bimetallic zeolitic imidazolate frameworks (ZIFs) for aqueous catalysis: Co/Zn-ZIF-8 as a cyclic-durable catalyst for hydrogen peroxide oxidative decomposition of organic dyes in water, RSC Adv. 12 (2022) 6025–6036, https://doi.org/10.1039/D2RA00218C.
[36] S. Frank, M. Folkjær, M.L.N. Nielsen, M.J. Marks, H.S. Jeppesen, M. Ceccato, S.J. L. Billinge, J. Catalano, N. Lock, Correlating the structural transformation and properties of ZIF-67 during pyrolysis, towards electrocatalytic oxygen evolution, J. Mater. Chem. A 12 (2024) 781–794, https://doi.org/10.1039/D3TA05293A.
[37] A.I.A. Soliman, A.A. Abdel-Wahaba, H.N. Abdelhamid, Hierarchical porous zeolitic imidazolate frameworks (ZIF-8) and ZnO@N-doped carbon for selective adsorption and photocatalytic degradation of organic pollutants, RSC Adv. 12 (2022) 7075–7084, https://doi.org/10.1039/D2RA00503D.
[38] F. Marpaung, T. Park, M. Kim, J.W. Yi, J. Lin, J. Wang, B. Ding, H. Lim, K. Konstantinov, Y. Yamauchi, J. Na, J. Kim, Gram-scale synthesis of bimetallic ZIFs and their thermal conversion to nanoporous carbon materials, Nanomaterials 9 (12) (2019) 1796, https://doi.org/10.3390/nano9121796.
[39] M.Z. Iqbal, M. Shaheen, U. Aftab, Z. Ahmad, M.Y. Solangi, M.I. Abro, S. M. Wabaidur, Faradically dominant pseudocapacitive manganese cobalt oxide electrode materials for hybrid supercapacitors and electrochemical water splitting, Energ. Fuel. 38 (2024) 2416–2425, https://doi.org/10.1021/acs.energyfuels.3c03444.
[40] H.S. Kim, J. Cook, H. Lin, J.S. Ko, S.H. Tolbert, V. Ozolins, B. Dunn, Oxygen vacancies enhance pseudocapacitive charge storage properties of MoO_{3-x}, Nat. Mater. 16 (2017) 454–460, https://doi.org/10.1038/nmat4810.
[41] J. Park, K. Kim, E. Lim, J. Hwang, Tuning internal accessibility via nanochannel orientation of mesoporous carbon spheres for high-rate potassium-ion storage in hybrid supercapacitors, Adv. Funct. Mater. 35 (2025) 2410010, https://doi.org/10.1002/adfm.202410010.
[42] Y. Yoon, B. Yan, Y. Surendranath, Suppressing ion transfer enables versatile measurements of electrochemical surface area for intrinsic activity comparisons, J. Am. Chem. Soc. 140 (2018) 2397–2400, https://doi.org/10.1021/jacs.7b10966.
[43] J.S. Sagu, D. Mehta, K.G.U. Wijayantha, Electrocatalytic activity of CoFe2O4 thin films prepared by AACVD towards the oxygen evolution reaction in alkaline media, Electrochem. Commun. 87 (2018) 1–4, https://doi.org/10.1016/j.elecom.2017.12.017.
[44] C. Masarapu, H.F. Zeng, K.H. Hung, B. Wei, Effect of temperature on the capacitance of carbon nanotube supercapacitors, ACS Nano 3 (2009) 2199–2206, https://doi.org/10.1021/nn900500n.
[45] C.C.L. McCrory, S. Jung, J.C. Peters, T.F. Jaramillo, Benchmarking heterogeneous electrocatalysts for the oxygen evolution reaction, J. Am. Chem. Soc. 135 (2013) 16977–16987, https://doi.org/10.1021/ja407115p.
[46] J.C. Wu, J.Y. Chang, X. Yuan, E. Khan, Y.S. Ok, C.H. Hou, Upcycling waste polyethylene terephthalate (PET) bottles into high-performance activated carbon for electrochemical desalination, Chemosphere 364 (2024) 143029, https://doi.org/10.1016/j.chemosphere.2024.143029.
[47] M. Ramadan H. M. A. Hassan A. Shahat R. F. M. Elshaarawy N. K. Allam Ultrahigh performance of novel energy-efficient capacitive deionization electrodes based on 3D nanotubular composites New J. Chem. 42 3560 https://doi.org/10.1039/C7NJ03838K.
[48] O. Noonan, Y. Kong, Y. Liu, M. Kalantari, A.K. Nanjundan, X. Huang, C. Yu, Hierarchical porous nitrogen-doped spray-dried graphene for high performance capacitive deionization, Adv. Energ. Sustain. Res. 3 (2022) 2100190, https://doi.org/10.1002/aesr.202100190.
[49] M. Kim, X. Xu, R. Xin, J. Earnshaw, A. Ashok, J. Kim, T. Park, A.K. Nanjundan, W. A. El-Said, J.W. Yi, J. Na, Y. Yamauchi, KOH-activated hollow ZIF-8 derived porous carbon: nanoarchitectured control for upgraded capacitive deionization and supercapacitor, ACS Appl. Mater. Interf. 13 (2021) 52034–52043, https://doi.org/10.1021/acsami.1c09107.
[50] K.K. Lee, W.S. Chin, C.H. Sow, Cobalt-based compounds and composites as electrode materials for high-performance electrochemical capacitors, J. Mater. Chem. A 2 (2014) 17212–17248, https://doi.org/10.1039/C4TA02074J.
[51] E. Budiyanto, H. Tüysüz, Cobalt oxide nanowires with controllable diameters and crystal structures for the oxygen evolution reaction, Eur. J. Inorg. Chem. (18) (2022) e202200065, https://doi.org/10.1002/ejic.202200065.
[52] S. Adhikari, S. Selvaraj, S.H. Ji, D.H. Kim, Encapsulation of Co3O4 nanocone arrays via ultrathin NiO for superior performance asymmetric supercapacitors, Small 16 (2020) 2005414, https://doi.org/10.1002/smll.202005414.
[53] E. Payen, J. Grimblot, S. Kasztelan, Study of oxidic and reduced alumina-supported molybdate and heptamolybdate species by in situ laser Raman spectroscopy, J. Phys. Chem. 91 (1987) 6642–6648, https://doi.org/10.1021/j100311a018.
[54] A.E. Islam, M.A. Susner, J. Carpena-Núñez, T.C. Back, R. Rao, J. Jiang, R. Pachter, S.A. Tenney, J.J. Boeckl, Be. Maruyama, Defect engineering of graphene using electron-beam chemistry with radiolyzed water, Carbon 166 (2020) 446–455, https://doi.org/10.1016/j.carbon.2020.04.098.
[55] L. Han, K.G. Karthikeyan, M.A. Anderson, J.J. Wouters, K.B. Gregory, Mechanistic insights into the use of oxide nanoparticles coated asymmetric electrodes for capacitive deionization, Electrochim. Acta 90 (2013) 573–581, https://doi.org/10.1016/j.electacta.2012.11.069.
[56] E. Buncel, H.A. Joly, J.R. Jones, Proton transfer from imidazole, benzimidazole, and their 1-alkyl derivatives. FMO analysis of the effect of methyl and benzo substitution, Canadian J. Chem. 64 (6) (1986) 1240–1245, https://doi.org/10.1139/v86-206.
[57] P.H. Tewari, A.B. Campbell, Temperature dependence of point of zero charge of cobalt and nickel oxides and hydroxides, J. Coll. Interf. Sci. 55 (1976) 531–539, https://doi.org/10.1016/0021-9797(76)90063-1.
[58] Y.C. Kao, Y.J. Shih, C.P. Huang, The role of reversible and polarizable surface charge in the electro-sorption of NaCl electrolyte onto activated carbon-graphite electrode, Chem. Eng. J. 430 (2022) 132862, https://doi.org/10.1016/j.cej.2021.132862.
[59] S.M. Silva, A.M. Bond, Contribution of migration current to the voltammetric deposition and stripping of lead with and without added supporting electrolyte at a mercury-free carbon fibre microdisc electrode, Anal. Chim. Acta 500 (2003) 307–321, https://doi.org/10.1016/S0003-2670(03)00881-X.
[60] H.D. Watts, L. Tribe, J.D. Kubicki, Arsenic adsorption onto minerals: connecting experimental observations with density functional theory calculations, Minerals 4 (2) (2014) 208–240, https://doi.org/10.3390/min4020208.
[61] Z. Yin, J. Lützenkirchen, N. Finck, N. Celaries, K. Dardenne, H.C.B. Hansen, Adsorption of arsenic(V) onto single sheet iron oxide: X-ray absorption fine structure and surface complexation, J.Coll. Interf. Sci. 554 (2019) 433–443, https://doi.org/10.1016/j.jcis.2019.07.024.
[62] K. Bourikas, T. Hiemstra, W.H. Van Riemsdijk, Adsorption of molybdate monomers and polymers on titania with a multisite approach, J. Phys. Chem. B 105 (2001) 2393–2403, https://doi.org/10.1021/jp002267q.
[63] G. Ilangovan, K.C. Pillai, Electrochemical and XPS characterization of glassy carbon electrode surface effects on the preparation of a monomeric molybdate(VI)-modified electrode, Langmuir 13 (1997) 566–575, https://doi.org/10.1021/la960053n.
[64] E.M. Davis, A. Bergmann, C. Zhan, H. Kuhlenbeck, B.R. Cuenya, Comparative study of Co_3O_4(111), $CoFe_2O_4$(111), and Fe_3O_4(111) thin film electrocatalysts for the oxygen evolution reaction, Nat. Commun. 14 (2023) 4791, https://doi.org/10.1038/s41467-023-40461-0.
[65] C. Buttersack, Modeling of type II high-resolution sorption isotherms: evaluation of different approaches, Colloids Surf. A Physicochem. Eng. Asp. 650 (2022) 129489, https://doi.org/10.1016/j.colsurfa.2022.129489.
[66] G. Gryglewicz, J. Machnikowski, E. Lorenc-Grabowska, G. Lota, E. Frackowiak, Effect of pore size distribution of coal-based activated carbons on double layer capacitance, Electrochim. Acta 50 (2005) 1197–1206, https://doi.org/10.1016/j.electacta.2004.07.045.
[67] I. Saptiama, Y.V. Kaneti, B. Yuliarto, H. Kumada, K. Tsuchiya, Y. Fujita, V. Malgras, N. Fukumitsu, T. Sakae, K. Hatano, K. Ariga, Y. Sugahara, Y. Yamauchi, Biomolecule-assisted synthesis of hierarchical multilayered boehmite and alumina nanosheets for enhanced molybdenum adsorption, Chem. A Eur. J. 25 (2019) 4843, https://doi.org/10.1002/chem.201900177.
[68] I. Saptiama, Y.V. Kaneti, Y. Suzuki, K. Tsuchiya, N. Fukumitsu, T. Sakae, J. Kim, Y.-M. Kang, K. Ariga, Y. Yamauchi, Template-free fabrication of mesoporous alumina nanospheres using post-synthesis water-ethanol treatment of monodispersed aluminium glycerate nanospheres for molybdenum adsorption, Small 14 (2018) 1800474, https://doi.org/10.1002/smll.201800474.
[69] A.Y. Kurmysheva, M.D. Vedenyapina, S.A. Kulaishin, P. Podrabinnik, N.W. S. Pinargote, A. Smirnov, A.S. Metel, J.F. Bartolomé, S.N. Grigoriev, Adsorption removal of Mo(VI) from an aqueous solution by alumina with the subsequent regeneration of the adsorbent, Int. J. Mol. Sci. 24 (2023) 8700, https://doi.org/10.3390/ijms24108700.
[70] J.M. Nseke, J. Kabuba, I. Otunniyi, Adsorption of selected oxyanions from aqueous solution using benzethonium chloride modified zeolite 4A: artificial neural network approach, Microporous Mesoporous Mater. 382 (2025) 113395, https://doi.org/10.1016/j.micromeso.2024.113395.
[71] W. Sun, H.M. Selim, Kinetic modeling of pH-dependent molybdenum(VI) adsorption and desorption on iron oxide-coated sand, Soil Sci. Soc. Am. J. 83 (2019) 357–365, https://doi.org/10.2136/sssaj2018.11.0449.
[72] F. Matusoiu, A. Negrea, M. Ciopec, N. Duteanu, P. Negrea, P. Svera, C. Ianasi, Molybdate recovery by adsorption onto silica matrix and iron oxide based composites, Gels 8 (2) (2022) 125, https://doi.org/10.3390/gels8020125.
[73] A. Afkhami, Ra. Norooz-Asl, Removal, preconcentration and determination of Mo (VI) from water and wastewater samples using maghemite nanoparticles, Colloids Surf. A Physicochem. Eng. Asp. 346 (2009) 52–57, https://doi.org/10.1016/j.colsurfa.2009.05.024.
[74] B.C. Bostick, S. Fendorf, G.R. Helz, Differential adsorption of molybdate and tetrathiomolybdate on pyrite (FeS2), Environ. Sci. Technol. 37 (2003) 285–291, https://doi.org/10.1021/es0257467.
[75] S. Hassanpour, M. Taghizadeh, Rapid and selective separation of molybdenum ions using a novel magnetic Mo(VI) ion imprinted polymer: a study of the adsorption properties, RSC Adv. 6 (2016) 100248–100261, https://doi.org/10.1039/C6RA20422H.
[76] B. Verbinnen, C. Block, D. Hannes, P. Lievens, M. Vaclavikova, K. Stefusova, G. Gallios, C. Vandecasteele, Removal of molybdate anions from water by

adsorption on zeolite-supported magnetite, Water Environ. Res. 84 (2012) 753–760, https://doi.org/10.2175/106143012X13373550427318.
[77] R. Gamal, S.E. Rizk, N.E. El-Hefny, The adsorptive removal of Mo(VI) from aqueous solution by a synthetic magnetic chromium ferrite nanocomposite using a nonionic surfactant, J. All. Comp. 853 (2021) 157039, https://doi.org/10.1016/j.jallcom.2020.157039.
[78] Y.C. Chen, C. Lu, Kinetics, thermodynamics and regeneration of molybdenum adsorption in aqueous solutions with NaOCl-oxidized multiwalled carbon nanotube, J. Ind. Eng. Chem. 20 (2014) 2521–2527, https://doi.org/10.1016/j.jiec.2013.10.035.
[79] E.R. Nightingale Jr., Phenomenological theory of ion solvation. Effective radii of hydrated ions, J. Phys. Chem. 63 (9) (1959) 1381–1387, https://doi.org/10.1021/j150579a011.
[80] M.Y. Kiriukhin, K.D. Collins, Dynamic hydration numbers for biologically important ions, Biophys. Chem. 99 (2002) 155–168, https://doi.org/10.1016/S0301-4622(02)00153-9.
[81] K. Singh, G. Li, J. Lee, H. Zuilhof, B.L. Mehdi, R.L. Zornitta, L.C.P.M. de Sme, Divalent ion selectivity in capacitive deionization with vanadium hexacyanoferrate: experiments and quantum-chemical computations, Adv. Funct. Mater. 31 (2021) 2105203, https://doi.org/10.1002/adfm.202105203.